




ARTICLE

# Cell ratcheting through the Sbf RabGEF directs force balancing and stepped apical constriction

Hui Miao<sup>1</sup>, Timothy E. Vanderleest<sup>2</sup>, Cayla E. Jewett<sup>1</sup> , Dinah Loerke<sup>2</sup> , and J. Todd Blankenship<sup>1</sup> 

**During *Drosophila melanogaster* gastrulation, the invagination of the prospective mesoderm is driven by the pulsed constriction of apical surfaces. Here, we address the mechanisms by which the irreversibility of pulsed events is achieved while also permitting uniform epithelial behaviors to emerge. We use MSD-based analyses to identify contractile steps and find that when a trafficking pathway initiated by Sbf is disrupted, contractile steps become reversible. Sbf localizes to tubular, apical surfaces and associates with Rab35, where it promotes Rab GTP exchange. Interestingly, when *Sbf/Rab35* function is compromised, the apical plasma membrane becomes deeply convoluted, and nonuniform cell behaviors begin to emerge. Consistent with this, *Sbf/Rab35* appears to prefigure and organize the apical surface for efficient Myosin function. Finally, we show that *Sbf/Rab35/CME* directs the plasma membrane to Rab11 endosomes through a dynamic interaction with Rab5 endosomes. These results suggest that periodic ratcheting events shift excess membrane from cell apices into endosomal pathways to permit reshaping of actomyosin networks and the apical surface.**

## Introduction

Understanding how tissue and cell morphologies are shaped has required advances in microscopy techniques that permit rapid time-lapse imaging. With this enhanced temporal resolution, a key discovery has been that many processes that once appeared smoothly continuous are actually composed of many pulsed, discrete events (Martin et al., 2009; Solon et al., 2009; Rauzi et al., 2010; Fernandez-Gonzalez and Zallen, 2011; Sawyer et al., 2011; Roh-Johnson et al., 2012). The discontinuous nature of cell shaping has deep implications for the underlying processes and suggests initiation, termination, and stabilization phases. This is especially apparent in the behaviors of nonmuscle Myosin II-driven processes, in which actomyosin assemblies form, generate a contractile force that deforms cell shape, and then either disband or undergo a period of remodeling. Pulsatile force generation therefore raises a central question: once force generation terminates, how are resultant cell morphologies maintained? Potential answers to this question are varied and include actin turnover and the viscoelastic properties of the cortex (Clément et al., 2017), but a further possible link lies in the behaviors of the plasma membrane itself. If morphological processes coordinate membrane trafficking events with cytoskeletal force generation, there is the potential for lasting changes in cell shape to be achieved (Levayer et al., 2011; Jewett et al., 2017).

Invagination of the mesoderm in *Drosophila melanogaster* occurs through the formation of an anterior–posterior (A–P) elongated furrow on the ventral surface of the embryo (Martin and Goldstein, 2014). This primarily occurs through ventral epithelial cells constricting their apical surfaces to adopt a conical shape that then causes a buckling inward of the mesodermal anlagen (Leptin and Grunewald, 1990). Apical constriction is driven by actomyosin forces that are localized to the apical surface through Rho signaling pathways (Young et al., 1991; Barrett et al., 1997; Dawes-Hoang et al., 2005; Kölsch et al., 2007; Xie and Martin, 2015; Mason et al., 2016). Importantly, apical constriction was one of the first systems in which the pulsatile nature of these Myosin II networks was first appreciated (Martin et al., 2009), with different transcriptional inputs regulating contractile and stabilization phases. Subsequent work elegantly demonstrated how cycles of Myosin II phosphorylation and dephosphorylation permitted remodeling of contractile forces during apical constriction (Vasquez et al., 2014), but how these cytoplasmic forces connect to events at the membrane has been unclear.

Indeed, while the mechanochemical pathways that direct Myosin II activities have been extensively explored (Nikolaidou and Barrett, 2004; Dawes-Hoang et al., 2005; Martin et al., 2009; Mason et al., 2013), the membrane trafficking networks that function during apical constriction have been virtually

<sup>1</sup>Department of Biological Sciences, University of Denver, Denver, CO; <sup>2</sup>Department of Physics, University of Denver, Denver, CO.

Correspondence to J. Todd Blankenship: [todd.blankenship@du.edu](mailto:todd.blankenship@du.edu).

© 2019 Miao et al. This article is distributed under the terms of an Attribution–Noncommercial–Share Alike–No Mirror Sites license for the first six months after the publication date (see <http://www.rupress.org/terms/>). After six months it is available under a Creative Commons License (Attribution–Noncommercial–Share Alike 4.0 International license, as described at <https://creativecommons.org/licenses/by-nc-sa/4.0/>).

unstudied in the *Drosophila* embryo. Rab proteins and their associated guanine nucleotide exchange factors (GEFs) are key mediators of membrane trafficking and cytoskeletal function (Walch-Solimena et al., 1997; Imamura et al., 1998; Sonnichsen and Zerial, 1998; Hattula et al., 2002; Grosshans et al., 2006; Horgan and McCaffrey, 2012; Jean et al., 2012) and form a large family of trafficking-dedicated monomeric GTPase proteins. Endosomal pathways guided by Rab proteins receive membrane from the cell surface through clathrin-mediated endocytosis (CME) as well as additional endocytic mechanisms (Rodman and Wandinger-Ness, 2000; Naslavsky et al., 2003; Powelka et al., 2004; Allaire et al., 2013; Maldonado-Báez et al., 2013; Mayor et al., 2014). A common pathway in many cells is newly endocytosed material first arriving at Rab5 early endosomes and then being further trafficked to Rab11 recycling endosomes. In previous work during cell intercalation in *Drosophila*, we demonstrated that a select subset of the 31 *Drosophila* Rab proteins (Rab4, Rab5, Rab8, Rab11, Rab14, Rab23, Rab35, and Rab39) are expressed in the early embryo at levels that are detectable by live imaging. Here, we show that a RabGEF, Sbf, coordinates the activity of Rab35 during apical constriction in the ventral furrow. We study a range of scales that vary from detecting biochemical activities and molecular interactions between Sbf and Rab35 to contractile cellular behaviors to final tissue morphologies. After Sbf or Rab35 disruption, cell ratcheting is compromised and the apical surface is filled with bleb-like features. Cell areas become highly variable and A-P anisotropies are compromised, revealing that Sbf and Rab35 are essential for uniform tissue constriction. Consistent with this, Sbf/Rab35 appears to prefigure and organize the apical surface for efficient and balanced Myosin II network function.

## Results

### Sbf, a potential Rab35 GEF, has an apical localization during apical constriction

We previously identified a pathway centered on Rab35 that was required for processive cell intercalation (Jewett et al., 2017). However, the mechanisms that trigger the functioning of this pathway are unknown. As Rab35 is a member of the small GTPase Rab family, this suggests that a GEF must be responsible for initiating this pathway. Three potential Rab35 GEFs (CG18659, Stratum/CG7787, and Sbf) have been identified through systematic biochemical purifications (Guruharsha et al., 2011; Gillingham et al., 2014). As an initial starting point, we created N- and C-terminal EGFP fusions for each of these GEFs and imaged a previously constructed GFP:Sbf (Jean et al., 2012). None of the four CG18659 or Stratum GFP transgenes displayed a discrete localization in the early *Drosophila* embryo. However, Sbf, which was the top hit for Rab35 in a systematic analysis of Rab-interacting proteins (Gillingham et al., 2014), possessed a striking localization at cell apices during mesoderm invagination (Fig. 1, A and C). Punctate and tubular foci of GFP:Sbf were present at cell apices and displayed dynamic behaviors with an average lifetime of ~70 s (Fig. 1, D and E). These compartments are similar in their localization and dynamics to those observed for Rab35 (Jewett et al., 2017).

We then asked if these apical tubulated Sbf compartments are open to the extracellular space and whether they fill immediately with Alexa Fluor 568-dextran following injection into the perivitelline (extracellular) space of the embryo. Indeed, 87% of Sbf compartments colocalized with dextran and thus appear to represent infoldings of the plasma similar to the Rab35 tubules that form during cell intercalation (Fig. 1, F and G). Sbf compartments are also enriched apically in cells of the ventral furrow and possess a lower frequency of occurrence at cell-cell interfaces (Fig. 1 H). Sbf is an interesting multidomain protein with DENN, GRAM, coiled coil (CC), and pleckstrin homology (PH) domains (Jean et al., 2012, 2015; Fig. 1 B). Deleting either the PH or DENN-CC domains removed the ability of Sbf to localize to cell apices or the plasma membrane, and a DENN-GRAM domain rescue construct did not localize as well, potentially consistent with a function for the PH domain in directing Sbf to the plasma membrane (Figs. 1 C and S1 A). Thus, Sbf localizes to apical regions of invaginating mesodermal cells and is a candidate to act as the upstream activator for Rab35.

### Sbf and Rab35 localize to tubular infoldings at the apical plasma membrane

In a previous study (Jewett et al., 2017), we showed that Rab35 is present on ingressing tubules at the plasma membrane as well as on endosomal compartments during cell intercalation. We were therefore interested to see if similar distributions of Rab35 are present during apical constriction. To do so, we performed both immunogold transmission EM (TEM) and extracellular dextran labeling of Rab35 compartments (Fig. 2, A and J). GFP-coupled immunogold particles revealed that 61% of Rab35 localizes to large tubular structures at the apical surface, while 35% of the Rab35 signal is at internal endosomal-type structures (Fig. 2 B). Similar to our results with Sbf (Fig. 1, F and G), 77% of the Rab35 compartments were immediately filled with extracellular dextran (Fig. 2, J and K). We then determined the extent of colocalization between Sbf and Rab35. Between 72% and 89% of mCh:Rab35/GFP:Sbf puncta colocalize with each other (Fig. 2, C-E). As Sbf possesses a DENN domain, which commonly activates Rab GTPases, we were curious if Sbf only initiates the formation of Rab35 compartments or if it is present throughout a compartment's lifetime. Interestingly, Sbf is present during much of a Rab35 compartment's lifetime, potentially consistent with a rapid cycling of Rab35 and a requirement for Sbf to maintain compartmental identity (Fig. 2, F and G).

We then asked if Rab35 compartments were present when Sbf function is disrupted. There is a deep loss in both the number and size of Rab35 compartments when measured across the full time of furrow ingression in *Sbf* embryos (at 8 min; Fig. 2, H, I, and L). The number of dextran-labeled compartments is also deeply reduced in *Sbf*-compromised embryos (Fig. 2, J and K). However, at the initiation of gastrulation, there is an unusual burst of small cytoplasmic Rab35 compartments that is accompanied by the loss of apical plasma membrane-associated Rab35 (Fig. 2, H and J-L). This may indicate that in the absence of a plasma membrane GEF, Rab35 activity is redirected toward an internal endocytic compartment and would be consistent with the activity of a separate endosomal Rab35 GEF. All together,

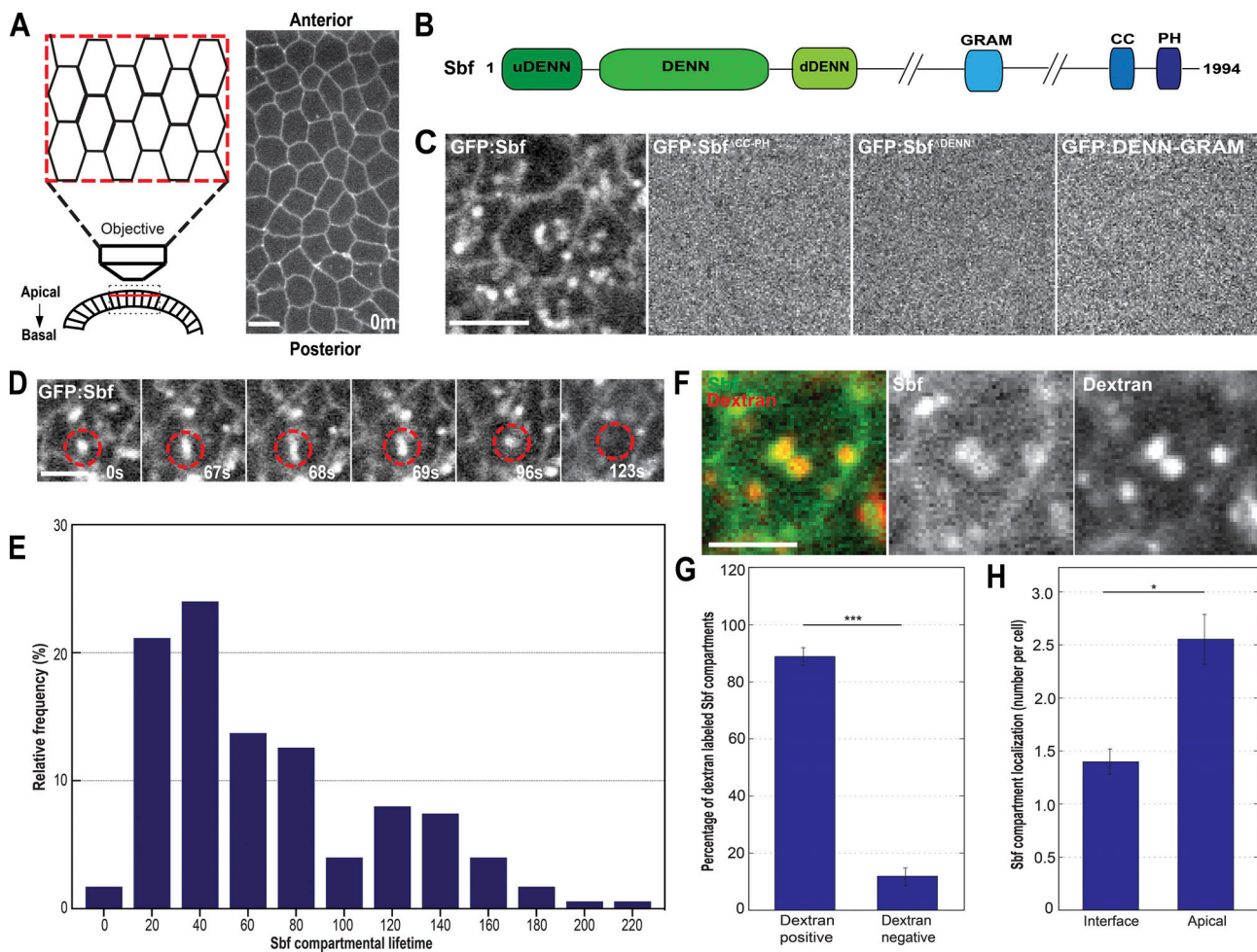


**Figure 1. A potential Rab35 GEF, Sbf, displays apical localization during *Drosophila* ventral furrow formation. (A)** Diagram of the imaging approach used to follow apical constriction of ventral furrow cells (left). Tangential z-slice of Resille:GFP; Spider:GFP from 2  $\mu$ m below the apical surface to show cell outlines (right; image is duplicate of Fig. 4 A control for schematic purposes). **(B)** Structural domain schematic of *Drosophila* Sbf protein. **(C)** Still frames of embryos expressing EGFP:Sbf, EGFP:Sbf<sup>ΔCC-PH</sup>, EGFP:Sbf<sup>ΔDENN</sup>, and EGFP:DENN-GRAM during ventral furrow formation. **(D)** Time-lapse images of an embryo expressing EGFP:Sbf. Images depicting the lifetime of a Sbf compartment: initiation of Sbf compartment (0 s), elongation phase (67 s), maximum point (68 s), shrinkage (69 s), and termination of a compartment (96 s). Dashed circle marks the indicated Sbf compartment. **(E)** Distribution of Sbf compartmental lifetimes.  $n = 175$  compartments. **(F)** Sbf compartments are colocalized with dextran immediately after injection. **(G)** Quantification of the number of dextran-labeled Sbf compartments during ventral furrow formation.  $n = 222$  compartments. **(H)** Quantification of the number of Sbf compartments on the interface or apical surface per cell.  $n = 132$  cells. Scale bars in A and C represent 5  $\mu$ m, and scale bars in D and F represent 2.5  $\mu$ m. Error bars indicate standard errors. Statistical significance was calculated using a Student's *t* test. \*,  $P < 0.05$ ; \*\*\*,  $P < 0.0005$ . In A, C, D, and F, embryos are oriented with anterior up and posterior down.

these results show that Rab35 and Sbf colocalize at the apical surface in plasma membrane-associated tubules and that Sbf function is essential for apical Rab35 localization.

**Sbf directly associates with Rab35 and increases GTP exchange rates**

As it was not possible to purify full-length Sbf protein, we tested if the putative Sbf GEF-DENN domain (amino acids 1–452) could directly associate with Rab35. Indeed, in vitro experiments demonstrated that MBP:Sbf-DENN could directly pull down Rab35 (Fig. 3, A and C). This displays a degree of specificity, as the recycling endosomal Rab11 was not pulled down by MBP:Sbf-DENN. Further, the interaction between Rab35 and Sbf-DENN is nucleotide dependent, as Rab35 loaded with a nonhydrolyzable GTP (GMP-PNP) is not

efficiently pulled down by MBP:Sbf-DENN (Fig. 3, B and C). We then examined if the DENN domain could promote Rab35 GTP exchange. Interestingly, in vitro Rab35 possesses a high intrinsic rate of exchange (Fig. 3, D and E). However, Sbf-DENN does promote a further increase in the rate of GTP exchange, which can be competed with excess GMP-PNP (Fig. 3, D and E). The observed GTP assay kinetics may represent the artificial conditions that an in vitro environment presents (the absence of a lipid bilayer, altered Rab-RabGEF binding geometries, or the absence of a RabGDI). Alternatively, these results are consistent with Rab35 being a rapid cycling small GTPase that requires an association with the RabGEF throughout the lifetime of a Rab35 compartment (Fig. 2 G). These results also establish that Sbf interacts with Rab35 directly and specifically in a GDP-dependent form.

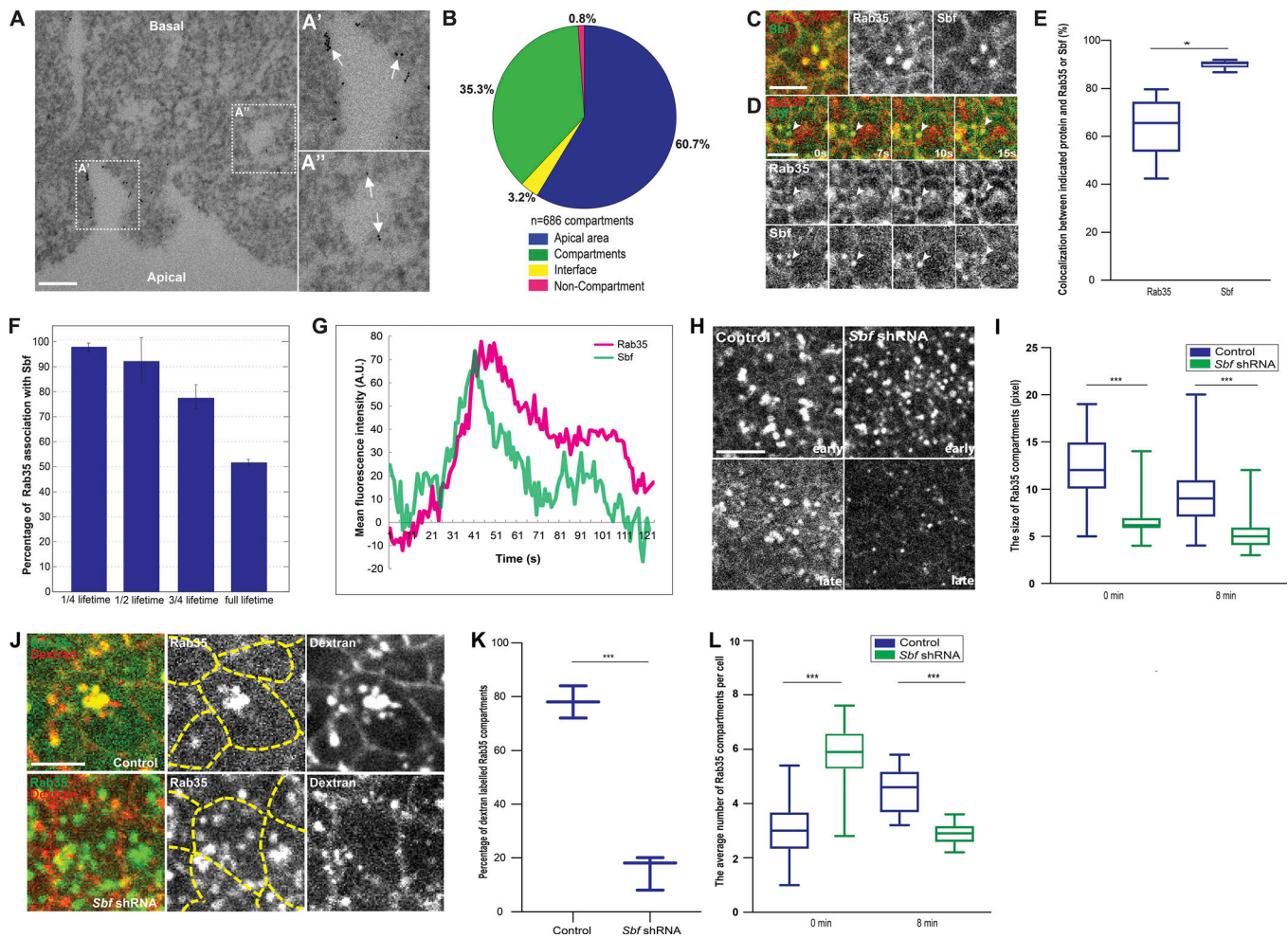


**Figure 2. Sbf associates with Rab35 in apically constricting cells.** (A, A', and A'') Immunogold TEM images of anti-GFP CRISPR:GFP:Rab35 demonstrates that Rab35 is present at apical surfaces and in large endosomal structures. (A' and A'') Magnification of area marked by dashed lines in A showing apical surface- (A') or endosomal structure-associated (A'') Rab35 immunogold compartments (arrows). (B) Quantification of Rab35 localization in A. (C) Time-lapse images of embryo expressing UAS:mCh:Rab35 (red) and UAS:EGFP:Sbf (green). mCh:Rab35 displays similar dynamics as CRISPR:GFP:Rab35 (see Materials and methods; Fig. S1, B and C). (D) The interaction between EGFP:Sbf (green) and mCh:Rab35 (red) over time. Arrowhead indicates colocalized Sbf and Rab35 compartment. (E) Percentage of colocalization between Rab35 and Sbf.  $n = 241$  (Rab35) and  $177$  (Sbf) compartments. (F) Sbf association with Rab35 over the lifetime of a Rab35 compartment.  $n = 190$  compartments. (G) Tracking of fluorescence intensity during the lifetime of a colocalized Rab35 and Sbf compartment. (H) Still frames of embryos expressing CRISPR:GFP:Rab35 in control or *Sbf* shRNA backgrounds during either early or late ventral furrow formation. (I) Quantification of the size of Rab35 compartments in control and *Sbf* shRNA embryos at early ( $t = 0$ ) and late ( $t = 8$  min) time points.  $n = 79$  (control, 0 min),  $101$  (*Sbf* shRNA, 0 min),  $171$  (control, 8 min), and  $169$  (*Sbf* shRNA, 8 min) compartments. (J) Images of embryo expressing CRISPR:GFP:Rab35 in either control or *Sbf* shRNA background injected with dextran into extracellular space. Very few Rab35 compartments are labeled with dextran when *Sbf* function is compromised. Yellow dashed line marks the cell outline. (K) Quantification of the labeled Rab35 compartments in J.  $n = 245$  (control) and  $312$  (*sbf* shRNA) compartments. (L) Quantification of the average number of Rab35 compartments in control and *Sbf* shRNA embryos.  $n = 433$  (control, 0 min),  $820$  (*Sbf* shRNA, 0 min),  $272$  (control, 8 min) and  $200$  (*Sbf* shRNA, 8 min) compartments. Scale bar in A represents  $200$  nm, scale bars in H and J represent  $5 \mu\text{m}$ , and scale bars in C and D represent  $2.5 \mu\text{m}$ . Statistical significance was calculated using Student's *t* test (K) or Mann-Whitney *U* test in (E, I, and L). \*,  $P < 0.05$ ; \*\*\*,  $P < 0.0005$ . In C, D, H, and J, embryos are oriented with anterior up and posterior down.

### Sbf is required for apical constriction

Given the striking apical dynamics of Sbf protein, we examined apical constriction during ventral furrow formation in *Sbf*-disrupted embryos. *Sbf* shRNA embryos failed to form a ventral invagination (Fig. 4, A and B; and Video 1), prompting a closer look at apical constriction rates. The overall rate of constriction was reduced by 32% in *Sbf*-disrupted embryos as compared with control embryos (Fig. 4, C and D); however, an interesting dynamic emerged when rates were broken down into initial, early, mid-, and late contractile periods. In initial

time points of apical constriction (0–120 s), constriction rates between wild-type and *Sbf*-disrupted cells are highly similar (Fig. 4 E). But as apical constriction proceeds, *Sbf*-compromised embryos display progressively stronger defects in constriction rates (Fig. 4, F–H). These disruptions in apical constriction led to deep defects in the overall flow of cells toward the ventral midline, with wild-type cells displacing significant distances in the course of invagination ( $19.5 \mu\text{m}$ ), while cells in *Sbf*-disrupted embryos possessed compromised displacements ( $7 \mu\text{m}$ ; Fig. 4, I and J). We also examined Rab35 function during these periods

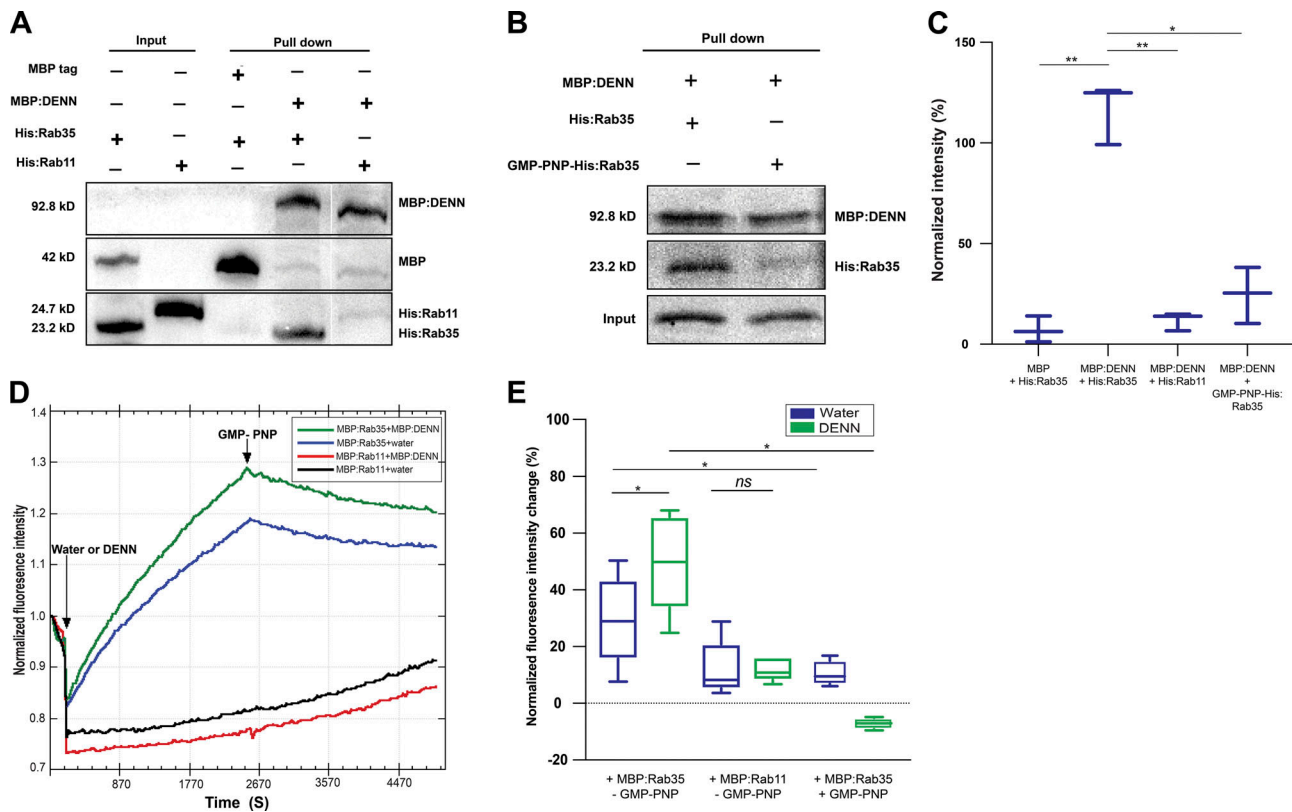


**Figure 3. Sbf promotes GTP exchange on Rab35 GTPase. (A)** Purified MBP:DENN pulls down His:Rab35, but not His:Rab11. **(B)** Preincubation of His:Rab35 with GMP-PNP decreases Rab35 pull-down by MBP:DENN. **(C)** Quantification of the normalized protein levels of His:Rab35, His:Rab11, and GMP PNP-His:Rab35 in pull-down assays in A and B. The intensity is normalized to MBP fusion protein band intensity. **(D)** GTP-exchange rates of Rab35 and Rab11 in the presence or absence of MBP:DENN. Adding unlabeled GMP-PNP (arrow) competes with the labeled GTP assay. Fluorescence was measured and normalized to the fluorescence at time 0 s. **(E)** Quantification of normalized fluorescence intensity changes in D ( $n = 5$  trials). Statistical significance was calculated using a Student's  $t$  test (C) and Wilcoxon test (E). \*,  $P < 0.05$ ; \*\*,  $P < 0.005$ .

and observed similar decreases in apical constriction rates and flow toward the ventral midline in *Rab35* shRNA embryos (Fig. 4, C, D, and K; and Video 1). Thus, Sbf and Rab35 are required after the initiation of apical constriction to permit the continued constriction of cell apices.

### The apical surface becomes deeply convoluted after Sbf/Rab35 disruption

As Sbf and Rab35 localize to the apical, tubular surface and disrupting their function compromised apical constriction, we probed the membrane ultrastructure of constricting cells. To do so, scanning EM was performed to image the apical surface in control and *Sbf*<sup>-</sup> or *Rab35*-disrupted embryos. Remarkably, scanning EM images show that *Sbf/Rab35*-disrupted embryos have surfaces that are deeply convoluted, with hundreds of bleb-like protrusions rising from the apical surface (Fig. 5, A and B). We also imaged embryos by TEM to obtain cross sections of ventral furrow cells through the apical-basal axis (Fig. 5 C). Again, these data revealed a highly convoluted surface. This also permitted the measurement of surface areas. *Sbf/Rab35* ventral furrow cells had greatly increased apical areas as compared with control cells (Fig. 5 D). These results are consistent with a failure to properly remodel and organize the apical surface when either *Sbf* or *Rab35* function is compromised.

### Automated identification of cell steps in the invaginating mesoderm by mean square displacement (MSD)-based analysis

Given the observed apical defects, we examined how these apical changes could influence the generation of pulsed, contractile steps. We therefore developed a method to identify periods of active motion based on the analysis of MSDs (see Materials and methods). As a first application, we compared apical area steps during apical constriction to the reversible area oscillations that occur in intercalating cells of the germband. In wild-type cells of the invaginating mesoderm, contractile steps are prolonged, with mean steps of ~60 s and area loss of  $0.16 \mu\text{m}^2/\text{s}$  (Fig. S2, A–E). This is in contrast to contractions in the germband in which area contractile steps have a mean step duration of ~40 s (Fig. S2, A, D, and E) with interface length changes of  $0.02 \mu\text{m}/\text{s}$  (Jewett et al., 2017). Area oscillations in the germband also display different contractile efficiencies, with total contraction rates of  $0.07 \mu\text{m}^2/\text{s}$  and contraction-only steps of  $0.11 \mu\text{m}^2/\text{s}$  (Vanderleest et al., 2018; Fig. S2, A–C). By these quantitative criteria, periods of active contraction in the ventral furrow are more sustained and possess higher rates than the reversible oscillations in apical area that occur during cell intercalation in the adjacent ventrolateral ectoderm. Given these differences, we were interested in quantifying the nature of cell ratcheting during apical constriction when *Sbf*- and *Rab35*-direct trafficking is compromised.

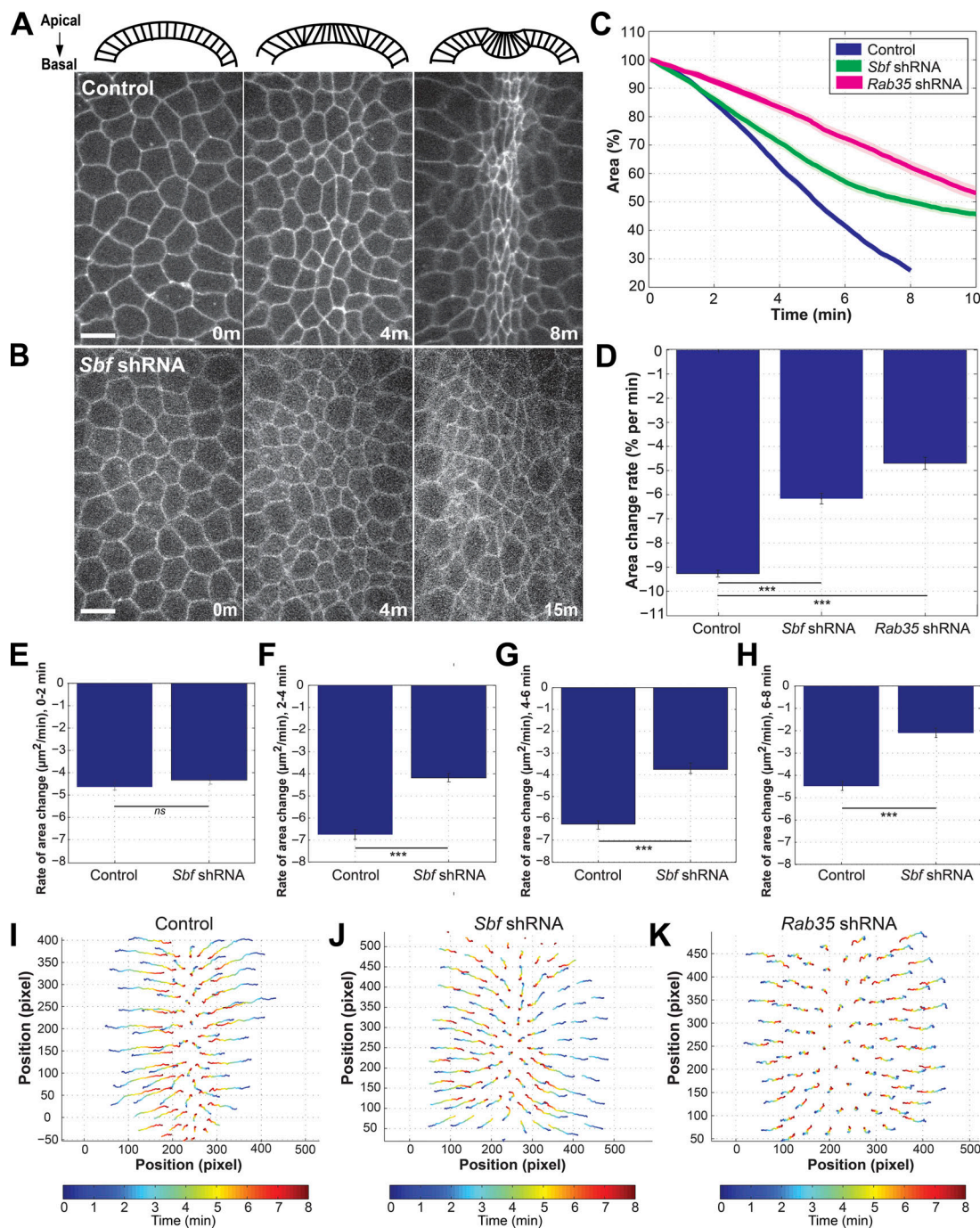
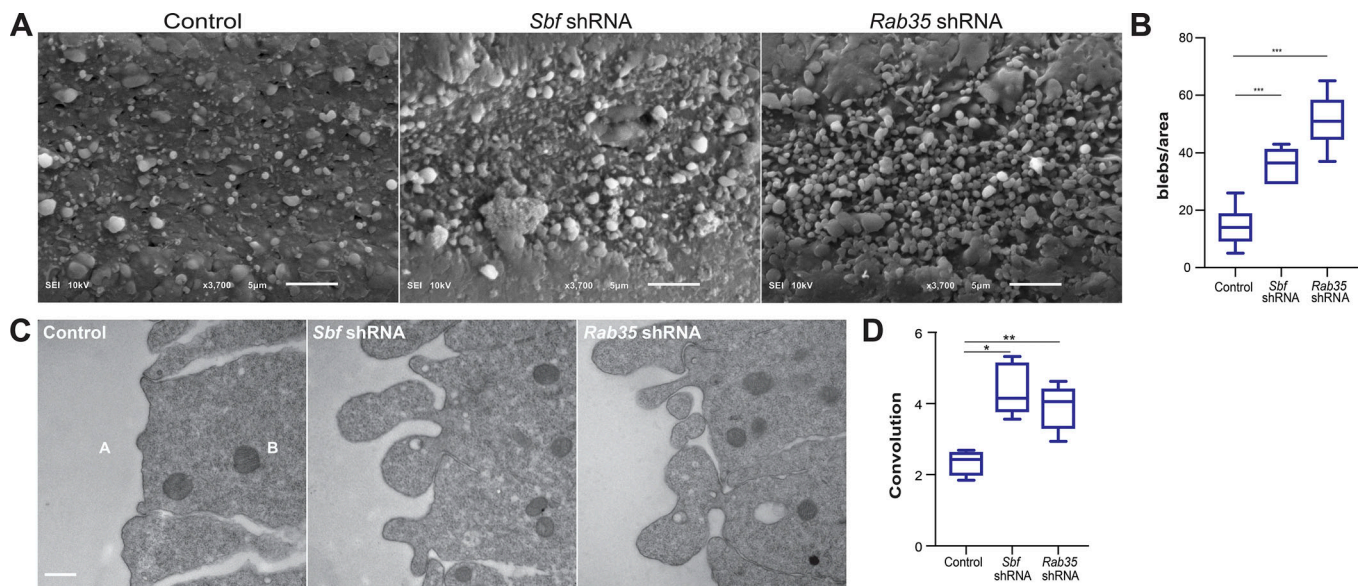


Figure 4. **Sbf** function is required for apical constriction. (A) YZ cross sections (schematic, top) and XY still images (bottom) of cell outlines revealed with Spider:GFP during ventral furrow formation. (B) Still images of embryos expressing Spider:GFP in *Sbf* shRNA background during ventral furrow formation. (C) Quantification of cell area change over time in control, *Sbf* shRNA, and *Rab35* shRNA backgrounds. (D) Quantification of the absolute rate of area change in control, *Sbf* shRNA, and *Rab35* shRNA embryos. (C and D)  $n = 3$  (control), 4 (*Sbf* shRNA), and 3 (*Rab35* shRNA) embryos. (E–H) Absolute rate of cell area change in control and *Sbf* shRNA embryos during 0–2 min (E), 2–4 min (F), 4–6 min (G), and 6–8 min (H). (E–H)  $n = 152$  (control), 196 (*Sbf* shRNA), and 216 (*Rab35* shRNA) cells. (I–K) Examples of control (I), *Sbf* shRNA (J), and *Rab35* shRNA (K) cell centroid trajectories movement traced over 8 min during ventral furrow formation. Time is color-coded (see color bar at the bottom). Scale bars represent 5  $\mu\text{m}$ . Error bars indicate standard errors. Statistical significance was calculated using a Student's *t* test. \*\*\*,  $P < 0.0005$ . In A and B, embryos are oriented with anterior up and posterior down.

### Sbf is essential for ratcheted apical constriction

As the initiation of apical constriction appeared normal in *Sbf*-disrupted embryos, we examined contractile step behaviors. As discussed above, wild-type cells cycle through periods of contractile stepping and stable behaviors (Fig. 6, A and B). *Sbf*- and

*Rab35*-disrupted cells still possessed contractile steps (Fig. 6, A, C, and D) but possessed slightly decreased step durations (Fig. 6, E and F). Intriguingly, however, expansion periods are present in *Sbf* and *Rab35* embryos that are not present in wild-type cells (green, Fig. 6, A–D). This was apparent when the number of



**Figure 5. Sbf and Rab35 are required to remodel the apical surface during constriction.** (A) Scanning EM images of control, *Sbf* shRNA, and *Rab35* shRNA embryos during ventral furrow formation. Embryos are oriented with anterior left and posterior right. (B) Number of bleb-like structures (minimum 0.16  $\mu\text{m}$  and maximum 1.6  $\mu\text{m}$  in size) in a 45  $\mu\text{m}^2$  area imaged by scanning EM. (C) TEM images of the apical surface in control, *Sbf* shRNA, and *Rab35* shRNA embryos. "A" and "B" markings indicate apical and basal portions of the cell, respectively. (D) Quantification of the convolution metric (the measured surface area divided by the linear length) in TEM images. Scale bar in C represents 400 nm. Statistical significance was calculated using a Mann–Whitney *U* test. \*,  $P < 0.05$ ; \*\*,  $P < 0.005$ ; \*\*\*,  $P < 0.0005$ .

reversing expansion steps that follow contractile steps was measured (Fig. 6 G), as well as the presence of a second peak in the region of positive area displacement (Fig. 6 H). These results demonstrate that *Sbf* and *Rab35* enforce a membrane ratcheting activity required for apical constriction.

### A requirement for cell ratcheting to maintain uniform furrow behaviors

Previous work has demonstrated that a gradient of forces is present across the incipient furrow during mesoderm invagination in *Drosophila* (Heer et al., 2017). As cells will experience different pulling forces across this gradient, we questioned whether a requirement for cell ratcheting would be equally present in apically constricting cells. To do so, we categorized cells by their distance from the ventral midline (the region of highest contractile forces) to the peripheral edges of the invaginating furrow (Fig. 7 A). Interestingly, there appears to be a higher requirement for ratcheting and *Sbf* function in cells closest to the ventral midline. Cells in the central regions of the ventral furrow had the deepest disruption in constriction rates, while peripherally located cells had near-wild-type, or even slightly greater than wild-type, rates (Fig. 7 B). This suggests that membrane ratcheting becomes increasingly important in tissue regions where cells are in an environment in which they are surrounded by high-force-generating neighbors.

Given the above defects in constriction rates, we then examined the effects of *Sbf* and *Rab35* function on cell shape in the ventral furrow. In wild-type furrows, apical constriction drives a narrowing of cells along the dorsal–ventral axis, such that cells shift from an isotropic configuration to an anisotropic shape that eventually achieves a uniform tissue configuration of

constricted cells that possess a longer axis aligned with the A–P axis (Martin et al., 2010). In 8 min, wild-type cells will shift to an aspect ratio that is  $\sim 2.2$  times longer along the A–P axis (Fig. 7, C and D). Instead, in *Sbf*- and *Rab35*-disrupted embryos, cells become increasingly more disordered, with a variety of apical cell sizes and orientations (Fig. 7, C–E). Cells with small apical surfaces are often juxtaposed to larger cells, and a “selfish” cell phenotype begins to emerge in which cells appear to constrict at the expense of neighboring cells (black-dotted cells, Fig. 7 C). This is also evident in a wider measured distribution of the standard deviation of cell areas (Fig. 7 E), and the organization of the overall tissue is disrupted as seen by the observed decreases in A–P aspect ratio (Fig. 7 D). At the individual cellular level, there is an  $\sim 25$ –30% increase in cells with larger apical surfaces ( $< 40 \mu\text{m}^2$ ) in *Sbf*- and *Rab35*-compromised embryos (Fig. 7 F). Interestingly, these large cells still possess step frequencies that are similar to cells in wild-type embryos, but they experience a greater degree of reversals that suggests they may not be able to consolidate gains and resist tissue pulling forces (Fig. 7, G and H). The reversals in area contractions then result in a reduced contraction rate (Fig. 7 I). These results suggest that cell ratcheting is required to permit proper force balancing between cells and to achieve uniform cell behaviors in the invaginating mesoderm.

### Sbf and Rab35 ratcheting behaviors guide Myosin II force generation

As the above results suggested that cell ratcheting is required to maintain an appropriate balancing of forces, we examined Myosin II behaviors in relation to *Rab35* and *Sbf* compartments. *Rab35* and *Sbf* puncta were often apparent in the same apical

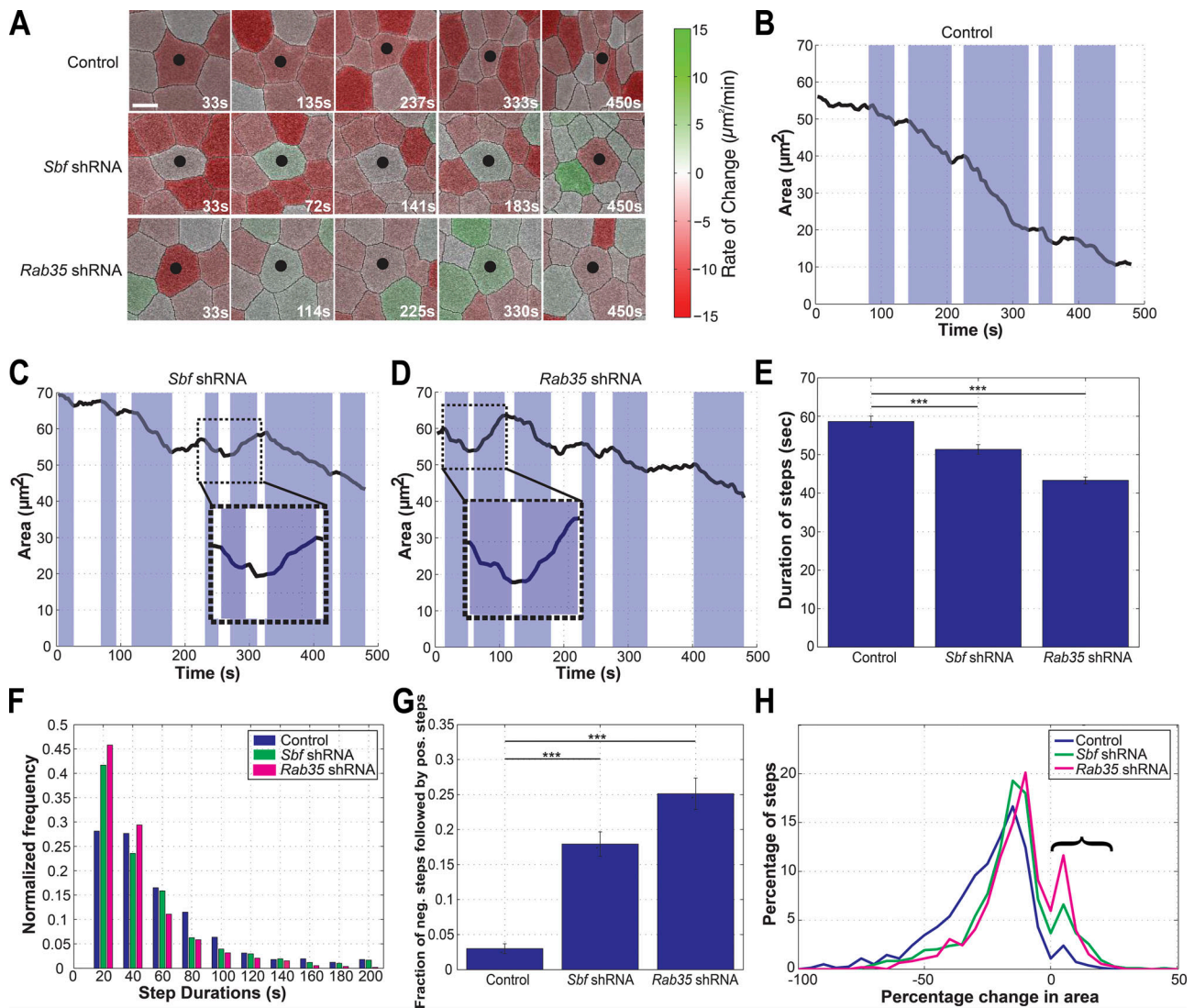


**Figure 6. Sbf and Rab35 work as a ratchet to ensure efficient apical constriction. (A)** Time-lapse images of individual cells in control, *Sbf* shRNA, and *Rab35* shRNA embryos during apical constriction. Expansion and constriction rates are color-coded (see color bar on the right). Red indicates constriction and green expansion. Central, black-dotted cells show expansion periods in *Sbf*- and *Rab35*-disrupted embryos that are not present in control. **(B–D)** Automated step detection of periods of active cell area change (shaded area) in control (B), *Sbf* shRNA (C), and *Rab35* shRNA embryos (D). **(E and F)** Duration (E) and frequency (F) of active steps in control, *Sbf* shRNA, and *Rab35* shRNA background. **(G)** Quantification of the fraction of negative steps followed by positive steps in control, *Sbf* shRNA, and *Rab35* shRNA embryos. **(H)** Quantification of active steps that cause area change. Bracket marks active but expanding steps. **(E–H)**  $n = 835$  steps from 167 cells (control), 1,090 steps from 237 cells (*Sbf* shRNA), and 1,109 steps from 223 cells (*Rab35* shRNA). Scale bar in A represents 5  $\mu\text{m}$ . Error bars indicate standard errors. Statistical significance was calculated using a Student's *t* test. \*\*\*,  $P < 0.0005$ . In A, embryos are oriented with anterior up and posterior down.

regions as Myosin II (Fig. 8 A). However, an interesting dynamic emerged when time-lapse movies were made. Rab35 puncta preceded Myosin II localization by ~45–60 s (Fig. 8 B and Video 2). This potential prefiguring of Myosin II concentrations was apparent regardless of GFP/RFP fluorophore combinations, and the degree of colocalization increased as Rab35 compartments matured (Fig. 8, B and C). Additionally, Rab35 compartments assembled just before the onset of apical constriction (Fig. S3, A and B). Given these results, we imaged Myosin II localization in *Sbf*- and *Rab35*-disrupted embryos. Overall intensities of Myosin II when measured across the entire epithelium were largely similar to wild type (Fig. 8 E), although comparably sized Rab35-

disrupted cells had a mild 11% decrease in Myosin II from wild-type while *Sbf* disruption led to a deeper 43% decrease in Myosin II (Fig. 8 L). Additionally, Myosin II organization appeared defective (Fig. 8 D). Myosin II displayed a greater degree of variability from cell to cell and was more asymmetrically distributed in the ingressing furrow (Fig. 8, I–K and M). Importantly, “selfish” cell behaviors were often correlated with a high/low juxtaposition of Myosin II localizing cells (asterisk, Fig. 8 D), and cell areas and Myosin II intensities displayed a direct correlation, but greater variability, in *Sbf* and *Rab35* compromised cells (Fig. 8, F–H and M). These results suggest that *Sbf*/*Rab35* compartmental and ratcheting-driven behaviors act as an



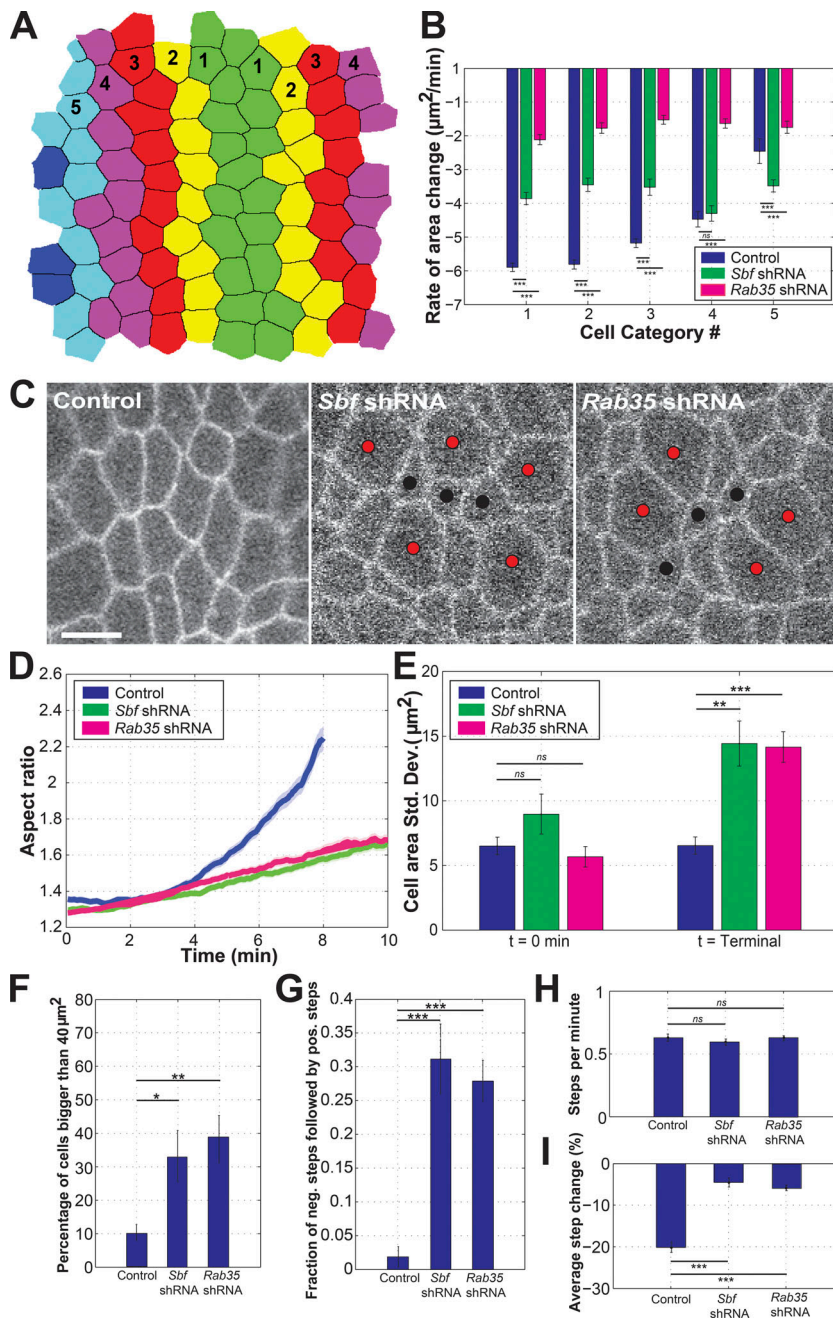


**Figure 7. Disruption of *Sbf* and *Rab35* function leads to unbalanced forces phenotype.** (A) Definition of cell categories (1–5, colored rows) based on distance from ventral midline. (B) Quantification of absolute rate of cell area change of different cell categories defined in A in control, *Sbf* shRNA, and *Rab35* shRNA background. Control cell numbers quantified from category 1 to 5 are  $n = 64, 65, 63, 31,$  and  $23,$  respectively; *Sbf* shRNA cell numbers are  $n = 93, 92, 76, 41,$  and  $36,$  respectively; and *Rab35* shRNA cell numbers are  $n = 87, 92, 88, 91,$  and  $65,$  respectively. (C) Cell outlines (Spider:GFP) in control, *Sbf* shRNA, and *Rab35* shRNA backgrounds by live imaging. Red dots and black dots mark large cells and small cells, respectively. Spider:GFP is heterozygous in *Sbf* and *Rab35* images. (D) Aspect ratio of cell shapes of control, *Sbf* shRNA, and *Rab35* shRNA embryos.  $n = 152$  (control),  $196$  (*Sbf* shRNA) and  $216$  (*Rab35* shRNA) cells. (E) Standard deviation of cell areas in control, *Sbf* shRNA and *Rab35* shRNA embryos.  $n = 379$  ( $t = 0$ , control),  $359$  ( $t =$  terminal, control),  $404$  ( $t = 0$ , *Sbf* shRNA),  $374$  ( $t =$  terminal, *Sbf* shRNA),  $419$  ( $t = 0$ , *Rab35* shRNA), and  $398$  ( $t =$  terminal, *Rab35* shRNA) cells. (F) The number of cells  $>40 \mu\text{m}^2$ .  $n = 324$  (control),  $79$  (*Rab35* shRNA), and  $89$  (*Sbf* shRNA) cells. (G) Quantification of contractile steps followed by expansion steps in big cells. (H) The number of steps per minute in big cells in control, *Sbf* shRNA, and *Rab35* shRNA embryos. (G and H)  $n = 33$  (control),  $23$  (*Sbf* shRNA), and  $29$  (*Rab35* shRNA) cells. (I) The quantification of change of average steps in big cells.  $n = 174$  (control),  $182$  (*Sbf* shRNA), and  $347$  (*Rab35* shRNA) steps. Scale bar represents  $5 \mu\text{m}$ . Error bars indicate standard errors. Statistical significance was calculated using a Mann–Whitney  $U$  test (B) and Student’s  $t$  test (E–I). \*,  $P < 0.05$ ; \*\*,  $P < 0.005$ ; \*\*\*,  $P < 0.0005$ . In A and C, embryos are oriented with anterior up and posterior down.

informational cue to direct Myosin II distributions in the ventral furrow.

**An endocytic pathway feeds plasma membrane to recycling endosomes during apical constriction**

The trafficking pathways that function during mesoderm invagination in *Drosophila* have been unexamined, so we focused on the function of CME, Rab5, Rab11, and Rab35 during apical constriction. We found that Rab35 compartments displayed transient interactions with both Rab5 early endosomes and Rab11 recycling endosomes (Fig. S4, A–C). While a higher percentage of Rab11 recycling endosomes displayed at least a partial colocalization with Rab35 compartments, Rab5 early endosomes displayed particularly active associations with Rab35 (Fig. S4, B

and C). We therefore wanted to determine if Rab35 is responsible for directing plasma membrane to Rab5 and Rab11 endosomal compartments. To test this, we disrupted CME through injection of two independent CME inhibitors. Disruption of CME did not change the number of Rab5 or Rab11 endosomes (Fig. 9, A–C) but did change the size and dynamics of endosomal compartments (Fig. 9, D–H; and Fig. S5, E–I). In particular, Rab11 endosomes became much smaller, consistent with a failure to deliver the membrane to the recycling endosome (Fig. 9, A, D, and E; and Fig. S5, E–G). Additionally, Rab5 endosomes often appeared to become stuck adjacent to Rab35 compartments at the cell surface, and Rab5 therefore displayed a more extensive colocalization with Rab35 in CME-disrupted embryos (Fig. 9, F–I; and Fig. S5, H and I). It is also interesting to note that

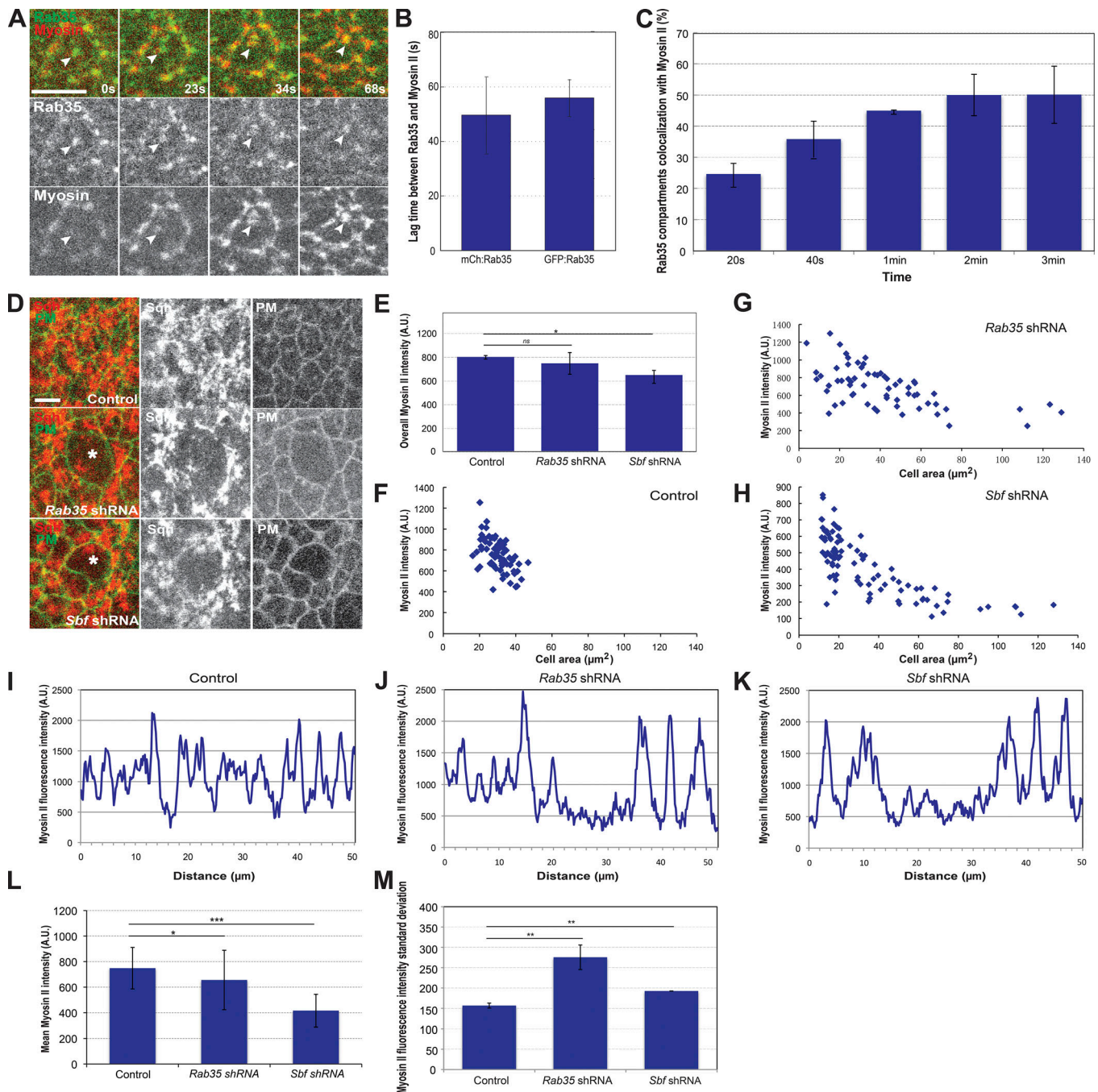


**Figure 8. *Sbf* and *Rab35* are required for Myosin II organization.** (A) Still frames from two-color live imaging of embryo expressing endogenous CRISPR: GFP:Rab35 (green) and mCherry:Sqh (red). Arrowhead indicates Rab35 compartment that precedes Myosin II localization. (B) Time lag between Rab35 and Myosin II appearance. Experiment was replicated with Rab35 in either the mCherry/red (left) or GFP/green (right) channel. GFP:Sqh or mCherry:Sqh was used in the opposing channel.  $n = 96$  (GFP:Rab35) and 36 (mCh:Rab35) compartments. (C) Percentage of colocalization between Rab35 compartments and Myosin II over time after formation of a Rab35 compartment.  $n = 163$  compartments. (D) Still images of Myosin II and plasma membrane (PM) outline marker in control, *Sbf* shRNA, and *Rab35* shRNA embryos (Resille:GFP, mCherry:Sqh). Asterisk marks big cell adjacent to "selfish" cells. (E) Mean Myosin II fluorescence tissue intensity during ventral furrow formation in control, *Sbf* shRNA, and *Rab35* shRNA embryos. (F–H) The distribution of Myosin II intensities and cell area sizes in individual control (F), *Rab35* shRNA (G), and *Sbf* shRNA cells (H).  $n = 67$  (control), 173 (*Rab35* shRNA), and 89 (*Sbf* shRNA) cells. (I–K) Line plot of Myosin II fluorescence intensity along A–P axis during ventral furrow formation in control (I), *Rab35* shRNA (J), and *Sbf* shRNA (K). (L) Mean Myosin II fluorescence intensity in 20–40  $\mu\text{m}^2$  big cells during ventral furrow formation.  $n = 61$  (control), 65 (*Rab35* shRNA), and 22 (*Sbf* shRNA) cells. (M) Standard deviation of average Myosin II intensity in control, *Rab35* shRNA, and *Sbf* shRNA cells. Scale bars in A and D represent 5  $\mu\text{m}$ . In bar plots, error bars indicate standard errors. Statistical significance was calculated using a Mann–Whitney  $U$  test (E and L) and a Student's  $t$  test (M). \*,  $P < 0.05$ ; \*\*,  $P < 0.05$ ; \*\*\*,  $P < 0.0005$ . In A and D, embryos are oriented with anterior up and posterior down.

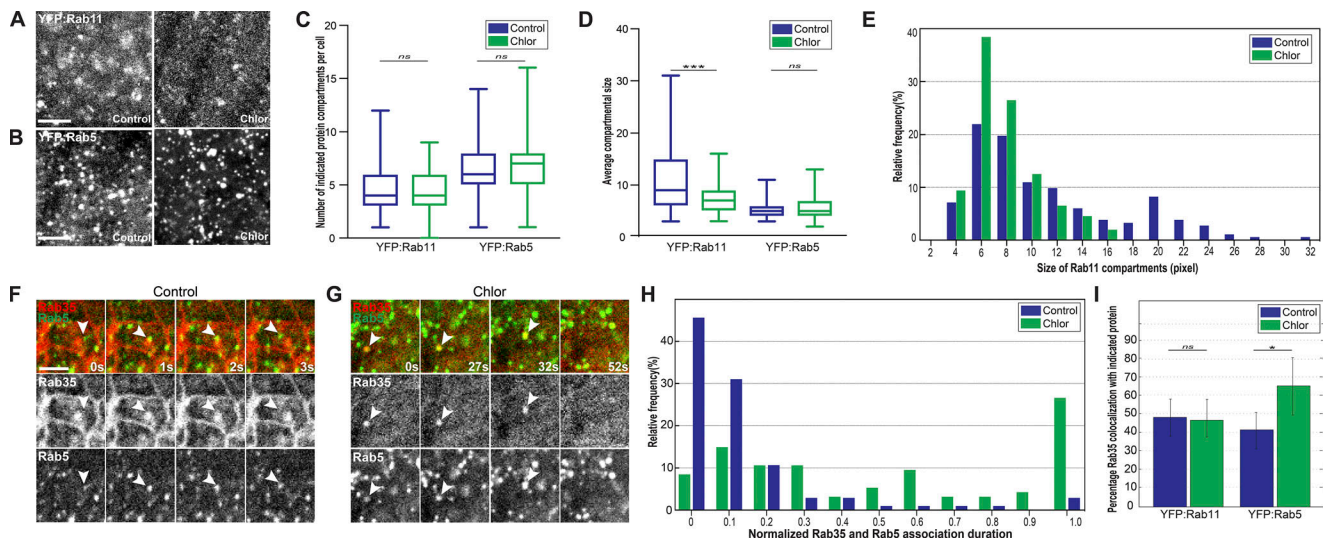


**Figure 9. CME is required for Rab35 and Rab5/Rab11 endosomal dynamics.** (A and B) Still frames of embryos expressing YFP:Rab11 (A) and YFP:Rab5 (B) injected with water control or chlorpromazine (chlor). (C) Quantification of the number of Rab5 and Rab11 compartments when injected with water control and chlorpromazine.  $n = 132$  (Rab5, control), 108 (Rab5, chlor), 118 (Rab11, control), and 124 (Rab11, chlor) cells. (D) Quantification of the size of Rab5 and Rab11 when injected with water control and chlorpromazine.  $n = 284$  (Rab5, control), 280 (Rab5, chlor), 258 (Rab11, control), and 350 (Rab11, chlor) compartments. (E) Distribution of Rab11 compartmental size in control and chlorpromazine injected embryos. (F and G) Images of the association between YFP:Rab5 and mCh:Rab35 in control (F) and chlorpromazine injected embryos (G). Arrowheads mark associated Rab5 and Rab35 compartments. Rab5 and Rab11 localization is largely unaffected by coexpression of mCh:Rab35 (Fig. S5, A–D). (H) Distribution of Rab35 and Rab5 normalized association times in control and chlorpromazine injected embryos. The association time was measured and normalized to each compartmental lifetime.  $n = 105$  (control) and 101 (chlor) compartments. (I) Quantification of the colocalization among Rab35, Rab11, and Rab5 in control and chlorpromazine-injected embryos.  $n = 113$  (Rab5, control), 160 (Rab5, chlor), 144 (Rab11, control), and 107 (Rab11, chlor) compartments. Scale bars in A, B, and F represent 5  $\mu\text{m}$ . In bar plots, error bars indicate standard errors. Statistical significance was calculated using a Mann-Whitney  $U$  test (C and D) and Student's  $t$  test (I). \*,  $P < 0.05$ ; \*\*\*,  $P < 0.0005$ . In A, B, F, and G, embryos are oriented with anterior up and posterior down.

coexpression of mCh:Rab35 led to slightly larger Rab11 endosomes (Fig. S5 A). However, disrupting Rab11 function by shRNA had no effect on ventral furrow formation, suggesting that it is the uptake of apical membrane, and not an indirect effect on recycling endosome function, that is the key Rab35 function during apical constriction (Fig. S5 J). These results suggest that Rab5 early endosomes associate with Rab35 compartments to potentiate membrane transfer to Rab11 recycling endosomes and the remodeling of the apical surface.

## Discussion

Whether and how trafficking networks function during apical constriction has not been clear. Here, we demonstrate that the Sbf RabGEF and Rab35 are essential for processive apical constriction and the formation of the ventral furrow. Sbf and Rab35 are present in tubular infoldings at the apical surface and coordinate cytoskeletal and membrane trafficking processes required for cell ratcheting during apical constriction. Rab35 directs membrane intake through CME to Rab5 early endosomes, while Sbf/Rab35 ratcheting directs the organization of Myosin II networks. In the absence of Sbf/Rab35 function, the apical surface fails to remodel and large, bleb-like structures create deeply convoluted surfaces. Additionally, processivity fails and apical constriction across the tissue loses uniformity and aberrant cell behaviors emerge, resulting in the disruption of ventral furrow formation. These results suggest that Sbf

generated Rab35 compartments represent a convergence of actomyosin and endocytic function.

## Nature of ratcheting

Apical constriction during *Drosophila* gastrulation is a classic system for the study of pulsed force generation that results in stepped contractile behaviors. When Sbf and Rab35 function are disrupted, contractile steps occur with near-wild-type dynamics; however, contractile steps are followed by periods of re-expansion of apical surfaces. A particularly revealing aspect of these disruptions in ratcheting is the behavior of Myosin II motor proteins at the tissue and cellular level. Overall levels of apical Myosin II are very similar between wild-type and Sbf/Rab35-compromised embryos. However, Myosin II distributions become highly variable, and wide deviations in cell areas and anisotropies are observed. These results suggest that cell ratcheting is particularly important in a multicellular and tissue-based context. As each epithelial cell is exerting contractile forces, a potential tug of war occurs within the tissue. In Sbf/Rab35-disrupted cells, it appears that forces become misbalanced, as cells selfishly constrict at the expense of large neighboring cells. Larger cells still possess contractile periods but are inefficient at maintaining constrictive gains. It is also intriguing that Sbf and Rab35 are present before Myosin II localization, consistent with a higher-order coordination between membrane ratcheting and actomyosin networks. It should also be noted that Myosin II levels are moderately decreased but

possess greater fractional variability in *Rab35*- and *Sbf*-disrupted embryos when cells of comparable sizes are measured, which may further contribute to the misbalancing of forces across the ventral epithelium.

What then is the nature of this underlying ratchet? We envision two possibilities: (1) a physical mechanism in which endocytic processes remove plasma membrane blebs of excess membrane during constriction that would otherwise interfere with the formation of a productive Myosin II network, or (2) a signaling mechanism in which *Sbf/Rab35* compartments are signaling hubs that guide cyclic recruitments of Myosin II motor proteins. These models are not mutually exclusive, and it is worth noting that recent work has shown that GPCR signaling activates Rho1-Myosin II through receptor clustering in membrane invaginations (Jha et al., 2018). However, the deep convolution of the apical surface after *Sbf/Rab35* disruption (as observed by scanning EM and TEM imaging) is certainly consistent with the first, physical mechanism model. Both models are also consistent with previous work demonstrating that reorganization of actomyosin networks (through F-actin turnover and cyclic Myosin II phosphorylation) is essential to maintain ratcheting and a balance of forces in the ventral furrow (Mason et al., 2013; Vasquez et al., 2014; Jodoin et al., 2015). It will be interesting to further examine if *Sbf/Rab35* has effects on the endocytic rates of the Mist/Smog GPCRs, which could further link their function to the organization of Myosin II networks.

#### **Sbf as a Rab35 GEF**

*Sbf* colocalizes with *Rab35* at the apical surface and physically interacts with *Rab35* in a GTP/GDP-dependent manner, with *Sbf* having a preferential binding for *Rab35* in its GDP state. This is a characteristic of RabGEF proteins and is consistent with the large tripartite DENN (uDENN/cDENN/dDENN) domain that is present in *Sbf*. The DENN domain of *Sbf* can also promote GDP-GTP exchange in *Rab35*. However, there are two interesting facets in the relationship between *Sbf* and *Rab35* that suggest some intriguing subtleties. When *Sbf* function is removed, there is a deep apical depletion of *Rab35*, but there is also an early burst of small *Rab35* cytoplasmic puncta that occurs at the beginning of ventral furrow formation. Our work indicates that *Rab35* is present both in endosomal and apical surface-associated populations. Additionally, although there is a high degree of colocalization between *Rab35* and *Sbf*, there are a small percentage of *Rab35* compartments that appear to lack *Sbf*. These results are consistent with the existence of a separate endosomal GEF for *Rab35*-associated endosomes. This could also suggest a competition between *Sbf* and the endosomal GEF for *Rab35* and may explain why an endosomal GEF would direct a burst of cytoplasmic, endosomal compartments in the absence of the apical *Sbf* GEF. These endosomal *Rab35* bursts may also indicate a deeper, underlying change in membrane trafficking pathways that occur at the initiation of apical constriction in the early embryo. The high intrinsic rate of GDP-GTP exchange by *Rab35* in vitro is also interesting. This could be a simple effect of the artificial conditions an in vitro environment presents, or it could also be consistent with *Rab35* functioning as a rapid cycling Rab GTPase protein. It is intriguing that *Sbf* is present

throughout much of the lifetime of an apical *Rab35* compartment and suggests that rapid cycles of GTP exchange are essential to remodel the apical surface and permit the proper generation of *Rab35* tubules. Alternatively, it may be that the absence of a RabGDI in in vitro assays causes nonrepresentative changes in GTP/GDP cycles. It will be interesting to further explore these differences in reconstitution assays in future work.

#### **Membrane trafficking and the constriction of cell surfaces**

Although the role that membrane trafficking pathways play in apical constriction during ventral furrow formation in *Drosophila* has been unclear, it is interesting to note that work in other systems has also implicated endosomal processes in apical constriction. For instance, a dominant-negative version of *Rab5* has been shown to interfere with apical constriction during the invagination of *Xenopus laevis* bottle cells, and disruption of the recycling endosomal protein *Rab11* inhibits apical surface contraction in neural folding, neural tube folding, and bottle cell formation (Lee and Harland, 2010; Ossipova et al., 2014, 2015). There have also been conflicting reports on the impact of disrupting trafficking pathways on actomyosin networks (Lee and Harland, 2010; Ossipova et al., 2014, 2015), but it is intriguing that during neural tube folding the accumulation of activated Myosin II is undetectable when *Rab11* function was compromised by either dominant-negative constructs or morpholino injection (Ossipova et al., 2014). These results suggest that there may be a conserved function by which endocytic membrane trafficking events are coordinated with cytoskeletal and contractile function to achieve apical constriction.

## **Materials and methods**

### **Cell segmentation**

Image and data analysis was performed in MATLAB. Cells were segmented using a seeded watershed algorithm and tracked in time. Cell area was measured as the sum of the pixels within the contour of the watershed segmentation lines converted to square microns. Additional segmentation analysis was performed as described in Jewett et al. (2017).

### **Cell categorization**

Cells are categorized based on the distance of their centroid from the ventral furrow midline and are numbered from 1 to 5, with 1 being nearest the midline. The position of the midline is defined at the beginning of furrow formation, time frame  $t_0$ , by a two-step process: (1) a line is drawn on the embryo at a point in time where the center of the furrow is discernable, and (2) the cells that were along that line are highlighted at frame  $t_0$  and the midline is drawn again across those cells. Next, the perpendicular distance of each cell's centroid to the midline is calculated, and the distances are binned to determine the category label. Bin width is calculated for each embryo separately as the average diameter of the cells at  $t_0$ . Cell diameter is calculated from the cell area with the approximation that the cells are circular.

### Step detection

To detect active motion steps in our vertex position trajectories, we used a rolling analysis window technique adapted from Huet et al. (2006). The MSD is the customary method to classify a subtrajectory into active, diffusive, or constrained motions based on whether the MSD curves upward, is linear, or curves downward, respectively. For periods of active motion, the MSD behaves as a power law  $MSD(\tau) \propto \tau^\gamma$ , where  $\gamma > 1$ . By calculating the parameter  $\gamma$  along a trajectory using a rolling window, we can identify periods of active and nonactive (i.e., either diffusive or constrained) motion. We chose a sliding window size of 57 s ( $n = 19$  frames), because it resulted in detected steps that were validated by controlled manual measurements. For each time window, we fit the MSD to lags between 4 and  $(N - 1)/2$  frames, where  $N$  is the odd-numbered number of points in the window. The first three lags were left out of the fitting, because localization error leads to artifactual subdiffusion at this short time scale lowering the value of  $\gamma$ . To reduce computation time, we performed linear fitting of the MSD versus  $\tau$  on a log-log plot. The determination of systematic from nonsystematic periods is made by setting a threshold on  $\gamma(t)$  of 1. We applied a minimum duration requirement of 20 s, because we found that positive detections below that duration did not represent real active periods.

### Cell aspect ratio

The aspect ratio of cell shape is calculated using the MATLAB *regionprops* function to obtain each cell's major and minor axes. The aspect ratio is defined as the major axis length divided by the minor axis length.

### Cell area standard deviation

The cell area standard deviation metric is a measure of how much variation in cell size there is at a given time point. For each embryo, the cell areas are normalized by the average area, and the standard deviation is taken. Then, the average and standard error is determined over individual embryos. This is done over just the first three cell categories. The terminal time represents the last time frame in which the cells were segmented.

### Fraction of negative followed by positive steps

The fraction of negative followed by positive steps is a measure of how many step reversals occur within a cell's time course. It is the ratio of the number of times a contraction (negative) step is immediately followed by an expansion (positive) step to the total number of contraction steps. The fraction of negative followed by positive steps can take values between 0 and 1, 0 if every step of a cell is a contraction and 1 if every contraction is followed by an expansion.

### Cell centroid trajectories

The centroid positions of cells are computed using MATLAB's *regionprops* function. The centroid trajectory images are produced with a couple modifications to the raw centroid positions. First, the positions are rotated such that the ventral furrow midline is vertical. Second, because in most cases the tissue tends drift in the direction of the A-P axis, we subtract this component of the drift. The A-P drift component is calculated as the average A-P motion of all the cells.

### Embryo processing for scanning EM, TEM, and immunogold TEM

For TEM and scanning EM sample preparation, OreR, *Sbf* shRNA, or *Rab35* shRNA embryos were dechorionated in 50% bleach solution and fixed for 20 min at the interface of heptane and 25% glutaraldehyde in 50 mM sodium cacodylate buffer (pH 7.4). Embryos were then postfixed in 1% OsO<sub>4</sub> and 50 mM cacodylate buffer (pH 7.4). The embryos were dried using hexamethyldisilazane for scanning EM preparation or were dehydrated and embedded in Embed 812 resin for TEM. Embryos were imaged on a JEOL JSM-6010LA scanning EM at 10 kV or a FEI Tecnai G2 Biotwin Transmission Electron Microscope at 80 kV.

For immunogold labeling, endogenous CRISPR:GFP:*Rab35* embryos were dechorionated in 50% bleach solution and fixed for 45 min at the interface of heptane and 16% formaldehyde in 50 mM sodium cacodylate buffer (pH 7.4). Embryos were manually devitellinized and stained with mouse anti-GFP (1:100, catalog no. A11120; Thermo Fisher Scientific) antibody and 6 nm gold-conjugated anti-mouse antibody (catalog no. 25124; Electron Microscopy Sciences) before embedding. Embryos were then postfixed in 1% OsO<sub>4</sub> and 50 mM cacodylate buffer (pH 7.4). Embryos were imaged on a FEI Tecnai G2 Biotwin TEM at 80 kV.

### Live imaging and injection

Embryos were dechorionated in 50% bleach solution for 2 min and then washed with water, staged on apple juice plates, and mounted with the ventral side up on a coverslip coated with heptane glue (3M double-sided tape dissolved in heptane). Embryos were covered with Halocarbon 27 oil. All imaging was performed on a CSU10b Yokogawa spinning-disk confocal from Zeiss and Solamere Technologies Group with a 63×/1.4 NA objective or a CSUX1FW Yokogawa spinning disk confocal from Nikon and Solamere Technologies Group with a 60×/1.4 NA objective. For drug or dye injection, following dechorionation and mounting as above, embryos were dehydrated for 12–15 min and then covered with Halocarbon 700 oil and injected with Chlorpromazine (10 mM, catalog no. C8138; Sigma), Pitstop2 (1.25 mM; Abcam), or Alexa Fluor 568-dextran (20 μg/ml, catalog no. D22912; Thermo Fisher Scientific). Injected embryos were imaged 20 min after chlorpromazine and Pitstop2 injection or immediately after Alexa Fluor 568-dextran injection.

### Protein preparation and pull-down assays

The DENN domain of *Sbf* or full-length *Rab35* or *Rab11* was amplified by PCR and cloned in-frame into pET-15b vector. The recombinant proteins were induced for 16 h at 20°C in *Escherichia coli* BL21 (DE3) using 1 mM IPTG. The bacteria were lysed by sonication and 6xHis- or MBP-tagged fusions were purified by incubation with Cobalt resin beads (catalog no. 89964; Thermo Fisher Scientific) or amylose resin beads (catalog no. E8021S; New England Biolabs), respectively. The recombinant proteins were eluted with 250 mM imidazole or 20 mM maltose in PBS buffer. Pull-down assays were performed by incubating 50 μg MBP fusions prebound to amylose resin beads for 1 h at room temperature with 6xHis fusions protein.

### GTP exchange assay

A RhoGEF Exchange Assay Biochemistry Kit (catalog no. BK100; Cytoskeleton) was used to do N-methylanthraniloyl (mant)-GTP exchange assays. Fluorescence spectroscopic analysis of mant-GTP incorporated by GTPase proteins was performed using a Tecan Infinite M1000 fluorescent spectrophotometer. 2  $\mu$ M GTPase protein (MBP:Rab35 and MBP:Rab11) were incubated in exchange buffer and mant-GTP for 3 min, after which water control or 2  $\mu$ M GEF (DENN domain of Sbf) was added. At 43 min, competing 1  $\mu$ l Guanosine 5'-[ $\beta$ , $\gamma$ -imido] triphosphate trisodium salt hydrate (GMP-PNP, catalog no. G0635; Sigma) was pipetted into the reaction to 10 mM. Reactions were monitored and recorded for 82.5 min with readings every 30 s.

### Time-lapse image editing and quantification

In box and whisker plots, the boxes represent 25th to 75th percentiles, the whiskers represent minimum to maximum, and the middle lines represent the medians.  $t = 0$  was set as the inflection point on apical area curves when apical constriction initiated. Spinning-disk images were edited with ImageJ or Photoshop, and images were leveled identically between samples. Myosin II fluorescence intensity was measured using ImageJ. Endogenous immunogold-labeled Rab35 compartments were calculated by counting gold particles in individual sections of images at 49,000 $\times$ . Apical surface-associated or interface-associated compartments are particles within 20 nm of apical surfaces or interfaces, respectively. Gold particles within 20 nm of vesicles or tubular structures were assigned as endosomal/cytoplasmic compartments. The quantity of gold particles localization at different places was expressed as the percentage of the total number of compartments. Colocalization between Rab35 and Sbf, Rab35 and Myosin II, and Rab35 and Rab5 or Rab11 was performed on time-lapse images. Rab35 puncta  $\geq 2$  pixels (Solamere spinning disk; pixel size = 0.164  $\mu$ m/pixel) were selected. The selected puncta were then overlaid with the opposing channel. When the overlapping region was equal or larger than  $2 \times 2$  pixels, the relationship between two proteins was determined as "colocalized." Average colocalization was found by performing a weighted average calculation from images collected from three different embryos, and standard deviations were plotted. Quantification of association times between Rab35 and Sbf, Rab35 and Myosin II, and Rab35 and Rab5 was performed using ImageJ on time-lapse images. Rab35 puncta were selected, tracked, and overlapped with the opposing channel over a compartment's lifetime. When the overlapping region was  $\geq 1 \times 1$  pixel and the overlapping period was  $\geq 1$  s, the relationship between two proteins was determined as "associated." Lag time between Rab35 and Myosin II is defined as the duration between the appearance of Rab35 and the start time point of association.

### Embryo fixation and immunostaining

Embryos were dechorionated in 50% bleach solution for 2 min and fixed for 1 h 10 min at the interface of heptane and 4% formaldehyde. Embryos were then manually devitelinized and stained with Alexa Fluor 546-phalloidin (1:200; Molecular Probes) and Rabbit anti-GFP (1:1,000; Invitrogen). Alexa Fluor

488 (1:500; Molecular Probes)-conjugated secondary antibodies were used. Embryos were mounted in Prolong Gold with DAPI (Molecular Probes).

### Fly stocks and genetics

The following fly stocks were used in this study: UAS-Sbf TRiP Valium 20 (57301), UAS-Sbf TRiP Valium 20 (44004), UAS-Sbf TRiP Valium 20 (32419), UAS-YFP:Rab35 9821, UASp-YFP:Rab5 24616, UASp-YFP:Rab11 9790 (all from the Bloomington *Drosophila* Stock Center); Spider:GFP (Szeged stock center); mCherry:Sqh (a gift from A. Martin, Massachusetts Institute of Technology, Cambridge, MA); CRISPR GFP:Rab35, UAS-mCh:Rab35 (Jewett et al., 2017); UAS:EGFP:Sbf, UAS:EGFP:SbfDENN/GRAM, UAS:EGFP:Sbf $\Delta$ CC-PH, and UAS:EGFP:Sbf $\Delta$ DENN (A. Kiger, University of California, San Diego, La Jolla, CA). UAS-mCh:Rab35 and CRISPR GFP:Rab35 display similar dynamics, although fewer mCh:Rab35 compartments were detected, consistent with the lower fluorescence from mCherry fluorophores as compared with EGFP (Fig. S1, B and C). UAS transgenic flies were crossed to  $\text{mat}\alpha\text{Tub-Gal4VP16 67C;15}$  (D. St. Johnson, Gurdon Institute, Cambridge, UK) maternal driver females, and second-generation embryos were analyzed. Embryos were collected from cages at 25°C, except embryos from Sbf TRiP Valium lines and the Rab35 Walium line, which were collected at 18°C. Consistent with shRNA knockdown with Valium 20 constructs, the penetrance of strongly defective Sbf shRNA embryos was  $\sim 50\%$  in different crosses and trials, and two different shRNA constructs (44004 and 32419) produced similar defects. Embryos have a higher penetrance in Resille:GFP, mCh:Sqh; Sbf shRNA. The penetrance of strongly defective embryos in Rab35 shRNA is  $\sim 40\%$ , although the remaining embryos often have weaker gastrulation defects. The scored penetrance is the number of embryos that have strong defects and unsuccessful apical constriction during ventral furrow formation divided by the total embryos imaged with additional embryos possessing weaker ventral furrow defects. Rab35 Walium 22 shRNA was constructed using the following primers: forward, 5'-CTAGCAGTGCTTCGATCATCTATTCAAGTTAGTTATATTCAAGCATATTGATAGATGATCGAAGCCGGCG-3'; and reverse, 5'-AATTCGCCGCTTCGATCATCTATTCAATATGCTTGAATATACTAACTTG AATAGATGATCGAAGCACTG-3'. Primers were annealed and cloned into pWALIU22 plasmid. All DNA constructs were validated by DNA sequencing.

### Repeatability

All measurements were quantified from a minimum of three embryos and represent at least two individual trials.

### Online supplemental material

Fig. S1 (related to Fig. 1) shows fixed cells of the various Sbf deletion constructs, which permits covisualization of cell outlines with phalloidin (F-actin), and compares endogenous GFP:Rab35 localization to that of UAS-mCh:Rab35. Fig. S2 compares contractile step dynamics during cell intercalation versus apical constriction. Fig. S3 demonstrates that Rab35 appears just before the onset of apical constriction. Fig. S4 reports on the degree of colocalization between Rab35 compartments with Rab5 early

endosomes or Rab11 recycling endosomes. Fig. S5 shows various data on how Rab35, CME, or Rab11 affects membrane trafficking dynamics or formation of the ventral furrow. Video 1 shows the disruption of apical constriction and ventral furrow formation in *Sbf*- and *Rab35*-compromised embryos as compared with a wild-type embryo. Video 2 demonstrates how Rab35 compartments (GFP) precede Myosin II recruitment (mCherry) to the apical surface.

## Acknowledgments

We are grateful to the generous colleagues who supplied antibodies and fly lines (A. Kiger, University of California, San Diego, San Diego, CA; A. Martin, Massachusetts Institute of Technology, Cambridge, MA). J. Bourne and the University of Colorado Anschutz TEM facility helped with immunogold TEM and sample preparation. Thanks are due to the Blankenship and Loerke laboratories for discussions and critical reading of the manuscript. Stocks obtained from the Bloomington *Drosophila* Stock Center (National Institutes of Health grant P40OD018537) were used in this study.

This work was supported by National Institutes of Health grants R01 GM090065, R01 GM127447, and R15 GM126422-01 to J.T. Blankenship and National Institutes of Health grants R01 GM127447 and R15 GM117463 and Research Corporation for Science Advancement Cottrell Scholar Award 2014 to D. Loerke.

The authors declare no competing financial interests.

Author contributions: The project was conceived by H. Miao, C.E. Jewett, and J.T. Blankenship. H. Miao performed *Sbf* live imaging, *Drosophila* genetics, drug injections and knockdown experiments, and molecular biology. T.E. Vanderleest performed automated analysis on *Sbf* and *Rab35* functionally disrupted embryos, and H. Miao analyzed compartment interface association. D. Loerke coded and advised on automated analysis. H. Miao performed dextran injections and compartment lifetime analysis. H. Miao and J.T. Blankenship designed research, analyzed data, and wrote the article.

Submitted: 11 May 2019

Revised: 5 August 2019

Accepted: 17 August 2019

## References

Allaire, P.D., M. Seyed Sadr, M. Chaineau, E. Seyed Sadr, S. Konefal, M. Foutouhi, D. Maret, B. Ritter, R.F. Del Maestro, and P.S. McPherson. 2013. Interplay between Rab35 and Arf6 controls cargo recycling to coordinate cell adhesion and migration. *J. Cell Sci.* 126:722–731. <https://doi.org/10.1242/jcs.112375>

Barrett, K., M. Leptin, and J. Settleman. 1997. The Rho GTPase and a putative RhoGEF mediate a signaling pathway for the cell shape changes in *Drosophila* gastrulation. *Cell*. 91:905–915. [https://doi.org/10.1016/S0092-8674\(00\)80482-1](https://doi.org/10.1016/S0092-8674(00)80482-1)

Clément, R., B. Dehapiot, C. Collinet, T. Lecuit, and P.F. Lenne. 2017. Viscoelastic dissipation stabilizes cell shape changes during tissue morphogenesis. *Curr. Biol.* 27:3132–3142.e4. <https://doi.org/10.1016/j.cub.2017.09.005>

Dawes-Hoang, R.E., K.M. Parmar, A.E. Christiansen, C.B. Phelps, A.H. Brand, and E.F. Wieschaus. 2005. folded gastrulation, cell shape change and the control of myosin localization. *Development*. 132:4165–4178. <https://doi.org/10.1242/dev.01938>

Fernandez-Gonzalez, R., and J.A. Zallen. 2011. Oscillatory behaviors and hierarchical assembly of contractile structures in intercalating cells. *Phys. Biol.* 8:045005. <https://doi.org/10.1088/1478-3975/8/4/045005>

Gillingham, A.K., R. Sinka, I.L. Torres, K.S. Lilley, and S. Munro. 2014. Toward a comprehensive map of the effectors of rab GTPases. *Dev. Cell*. 31:358–373. <https://doi.org/10.1016/j.devcel.2014.10.007>

Grosshans, B.L., D. Ortiz, and P. Novick. 2006. Rabs and their effectors: achieving specificity in membrane traffic. *Proc. Natl. Acad. Sci. USA*. 103:11821–11827. <https://doi.org/10.1073/pnas.0601617103>

Guruharsha, K.G., J.F. Rual, B. Zhai, J. Mintseris, P. Vaidya, N. Vaidya, C. Beekman, C. Wong, D.Y. Rhee, O. Cenaj, et al. 2011. A protein complex network of *Drosophila melanogaster*. *Cell*. 147:690–703. <https://doi.org/10.1016/j.cell.2011.08.047>

Hattula, K., J. Furuholm, A. Arffman, and J. Peränen. 2002. A Rab8-specific GDP/GTP exchange factor is involved in actin remodeling and polarized membrane transport. *Mol. Biol. Cell*. 13:3268–3280. <https://doi.org/10.1091/mbc.e02-03-0143>

Heer, N.C., P.W. Miller, S. Chanet, N. Stoop, J. Dunkel, and A.C. Martin. 2017. Actomyosin-based tissue folding requires a multicellular myosin gradient. *Development*. 144:1876–1886. <https://doi.org/10.1242/dev.146761>

Horgan, C.P., and M.W. McCaffrey. 2012. Endosomal trafficking in animal cytokinesis. *Front. Biosci. (Schol. Ed.)*. 4:547–555. <https://doi.org/10.2741/s284>

Huet, S., E. Karatekin, V.S. Tran, I. Fanget, S. Cribier, and J.P. Henry. 2006. Analysis of transient behavior in complex trajectories: application to secretory vesicle dynamics. *Biophys. J.* 91:3542–3559. <https://doi.org/10.1529/biophysj.105.080622>

Imamura, H., K. Takaishi, K. Nakano, A. Kodama, H. Oishi, H. Shiozaki, M. Monden, T. Sasaki, and Y. Takai. 1998. Rho and Rab small G proteins coordinately reorganize stress fibers and focal adhesions in MDCK cells. *Mol. Biol. Cell*. 9:2561–2575. <https://doi.org/10.1091/mbc.9.9.2561>

Jean, S., S. Cox, E.J. Schmidt, F.L. Robinson, and A. Kiger. 2012. *Sbf*/MTMR13 coordinates PI(3)P and Rab21 regulation in endocytic control of cellular remodeling. *Mol. Biol. Cell*. 23:2723–2740. <https://doi.org/10.1091/mbc.e12-05-0375>

Jean, S., S. Cox, S. Nassari, and A.A. Kiger. 2015. Starvation-induced MTMR13 and RAB21 activity regulates VAMP8 to promote autophagosome-lysosome fusion. *EMBO Rep.* 16:297–311. <https://doi.org/10.15252/embr.201439464>

Jewett, C.E., T.E. Vanderleest, H. Miao, Y. Xie, R. Madhu, D. Loerke, and J.T. Blankenship. 2017. Planar polarized Rab35 functions as an oscillatory ratchet during cell intercalation in the *Drosophila* epithelium. *Nat. Commun.* 8:476. <https://doi.org/10.1038/s41467-017-00553-0>

Jha, A., T.S. van Zanten, J.M. Philippe, S. Mayor, and T. Lecuit. 2018. Quantitative control of GPCR organization and signaling by endocytosis in epithelial morphogenesis. *Curr. Biol.* 28:1570–1584.e6. <https://doi.org/10.1016/j.cub.2018.03.068>

Jodoin, J.N., J.S. Coravos, S. Chanet, C.G. Vasquez, M. Tworoger, E.R. Kingston, L.A. Perkins, N. Perrimon, and A.C. Martin. 2015. Stable force balance between epithelial cells arises from F-actin turnover. *Dev. Cell*. 35:685–697. <https://doi.org/10.1016/j.devcel.2015.11.018>

Kölsch, V., T. Seher, G.J. Fernandez-Ballester, L. Serrano, and M. Leptin. 2007. Control of *Drosophila* gastrulation by apical localization of adherens junctions and RhoGEF2. *Science*. 315:384–386. <https://doi.org/10.1126/science.1134833>

Lee, J.Y., and R.M. Harland. 2010. Endocytosis is required for efficient apical constriction during *Xenopus* gastrulation. *Curr. Biol.* 20:253–258. <https://doi.org/10.1016/j.cub.2009.12.021>

Leptin, M., and B. Grunewald. 1990. Cell shape changes during gastrulation in *Drosophila*. *Development*. 110:73–84.

Levayer, R., A. Pelissier-Monier, and T. Lecuit. 2011. Spatial regulation of Dia and Myosin-II by RhoGEF2 controls initiation of E-cadherin endocytosis during epithelial morphogenesis. *Nat. Cell Biol.* 13:529–540. <https://doi.org/10.1038/ncb2224>

Maldonado-Báez, L., N.B. Cole, H. Krämer, and J.G. Donaldson. 2013. Microtubule-dependent endosomal sorting of clathrin-independent cargo by Hook1. *J. Cell Biol.* 201:233–247. <https://doi.org/10.1083/jcb.201208172>

Martin, A.C., and B. Goldstein. 2014. Apical constriction: themes and variations on a cellular mechanism driving morphogenesis. *Development*. 141:1987–1998. <https://doi.org/10.1242/dev.102228>

Martin, A.C., M. Kaschube, and E.F. Wieschaus. 2009. Pulsed contractions of an actin-myosin network drive apical constriction. *Nature*. 457:495–499. <https://doi.org/10.1038/nature07522>

Martin, A.C., M. Gelbart, R. Fernandez-Gonzalez, M. Kaschube, and E.F. Wieschaus. 2010. Integration of contractile forces during tissue

- invagination. *J. Cell Biol.* 188:735–749. <https://doi.org/10.1083/jcb.200910099>
- Mason, F.M., M. Tworoger, and A.C. Martin. 2013. Apical domain polarization localizes actin-myosin activity to drive ratchet-like apical constriction. *Nat. Cell Biol.* 15:926–936. <https://doi.org/10.1038/ncb2796>
- Mason, F.M., S. Xie, C.G. Vasquez, M. Tworoger, and A.C. Martin. 2016. RhoA GTPase inhibition organizes contraction during epithelial morphogenesis. *J. Cell Biol.* 214:603–617. <https://doi.org/10.1083/jcb.201603077>
- Mayor, S., R.G. Parton, and J.G. Donaldson. 2014. Clathrin-independent pathways of endocytosis. *Cold Spring Harb. Perspect. Biol.* 6:a016758. <https://doi.org/10.1101/cshperspect.a016758>
- Naslavsky, N., R. Weigert, and J.G. Donaldson. 2003. Convergence of non-clathrin- and clathrin-derived endosomes involves Arf6 inactivation and changes in phosphoinositides. *Mol. Biol. Cell.* 14:417–431. <https://doi.org/10.1091/mbc.02-04-0053>
- Nikolaidou, K.K., and K. Barrett. 2004. A Rho GTPase signaling pathway is used reiteratively in epithelial folding and potentially selects the outcome of Rho activation. *Curr. Biol.* 14:1822–1826. <https://doi.org/10.1016/j.cub.2004.09.080>
- Ossipova, O., K. Kim, B.B. Lake, K. Itoh, A. Ioannou, and S.Y. Sokol. 2014. Role of Rab11 in planar cell polarity and apical constriction during vertebrate neural tube closure. *Nat. Commun.* 5:3734. <https://doi.org/10.1038/ncomms4734>
- Ossipova, O., I. Chuykin, C.W. Chu, and S.Y. Sokol. 2015. Vangl2 cooperates with Rab11 and Myosin V to regulate apical constriction during vertebrate gastrulation. *Development.* 142:99–107. <https://doi.org/10.1242/dev.111161>
- Powelka, A.M., J. Sun, J. Li, M. Gao, L.M. Shaw, A. Sonnenberg, and V.W. Hsu. 2004. Stimulation-dependent recycling of integrin  $\beta 1$  regulated by ARF6 and Rab11. *Traffic.* 5:20–36. <https://doi.org/10.1111/j.1600-0854.2004.00150.x>
- Rauzi, M., P.F. Lenne, and T. Lecuit. 2010. Planar polarized actomyosin contractile flows control epithelial junction remodelling. *Nature.* 468:1110–1114. <https://doi.org/10.1038/nature09566>
- Rodman, J.S., and A. Wandering-Ness. 2000. Rab GTPases coordinate endocytosis. *J. Cell Sci.* 113:183–192.
- Roh-Johnson, M., G. Shemer, C.D. Higgins, J.H. McClellan, A.D. Werts, U.S. Tulu, L. Gao, E. Betzig, D.P. Kiehart, and B. Goldstein. 2012. Triggering a cell shape change by exploiting preexisting actomyosin contractions. *Science.* 335:1232–1235. <https://doi.org/10.1126/science.1217869>
- Sawyer, J.K., W. Choi, K.C. Jung, L. He, N.J. Harris, and M. Peifer. 2011. A contractile actomyosin network linked to adherens junctions by Cncaoe/afadin helps drive convergent extension. *Mol. Biol. Cell.* 22:2491–2508. <https://doi.org/10.1091/mbc.e11-05-0411>
- Solon, J., A. Kaya-Copur, J. Colombelli, and D. Brunner. 2009. Pulsed forces timed by a ratchet-like mechanism drive directed tissue movement during dorsal closure. *Cell.* 137:1331–1342. <https://doi.org/10.1016/j.cell.2009.03.050>
- Sonnichsen, B., and M. Zerial. 1998. Membrane dynamics of the pericentriolar recycling endosome monitored with Rab11-GFP. *Mol. Biol. Cell.* 9:464A.
- Vanderleest, T.E., C.M. Smits, Y. Xie, C.E. Jewett, J.T. Blankenship, and D. Loerke. 2018. Vertex sliding drives intercalation by radial coupling of adhesion and actomyosin networks during *Drosophila* germband extension. *eLife.* 7:e34586. <https://doi.org/10.7554/eLife.34586>
- Vasquez, C.G., M. Tworoger, and A.C. Martin. 2014. Dynamic myosin phosphorylation regulates contractile pulses and tissue integrity during epithelial morphogenesis. *J. Cell Biol.* 206:435–450. <https://doi.org/10.1083/jcb.201402004>
- Walch-Solimena, C., R.N. Collins, and P.J. Novick. 1997. Sec2p mediates nucleotide exchange on Sec4p and is involved in polarized delivery of post-Golgi vesicles. *J. Cell Biol.* 137:1495–1509. <https://doi.org/10.1083/jcb.137.7.1495>
- Xie, S., and A.C. Martin. 2015. Intracellular signalling and intercellular coupling coordinate heterogeneous contractile events to facilitate tissue folding. *Nat. Commun.* 6:7161. <https://doi.org/10.1038/ncomms8161>
- Young, P.E., T.C. Pesacreta, and D.P. Kiehart. 1991. Dynamic changes in the distribution of cytoplasmic myosin during *Drosophila* embryogenesis. *Development.* 111:1–14.